Journal of Materials Chemistry A

Accepted Manuscript

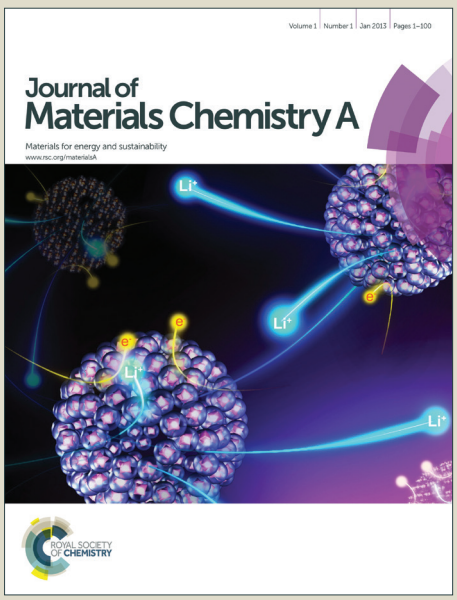

ROYAL SOCIETY OF CHEMISTRY

www.rsc.org/materialsA

Cite this: DOI: 10.1039/c0xx00000x

www.rsc.org/xxxxxx

ARTICLE TYPE

Heterostructured composites consisting of In_2O_3 nanorods and reduced graphene oxide with enhanced interfacial electron transfer and photocatalytic performance

Hui Huang [a,c], Zongkuan Yue [a], Gang Li [a], Xiaomei Wang [a], Jie Huang [a,b], Yukou Du [a] and Ping Yang* [a]

Received (in XXX, XXX) Xth XXXXXXXXX 20XX, Accepted Xth XXXXXXXXX 20XX
DOI: 10.1039/b000000x

A novel composite of In_2O_3 nanorods (INR) hybridized with reduced graphene oxide (RGO) was fabricated by a facile UV-assisted photoreduction method. The as-prepared samples were systematically characterized by X-ray diffraction, scanning electron microscopy, transmission electron microscopy, Raman spectroscopy, X-ray photoelectron spectroscopy and UV-vis diffuse reflectance spectroscopy techniques. The one dimensional INR with high surface-to-volume ratio anchored on the surface of RGO homogeneously, resulting in a nice interfacial contact between INR and RGO. The photocatalytic activities of the INR-RGO composites were investigated for 4-chlorophenol (4-CP) degradation under UV-vis or visible light irradiation. The photodegradation yield of the optimized photocatalyst reached 91.6% which was about 1.9 times as high as that of INR under visible light irradiation (> 400 nm). The enhanced photocatalytic activity of the INR-RGO composites can be ascribed to the efficiently interfacial charge transfer from INR to RGO, which resulted in the prolonged lifetime of the photoinduced charge carriers.

1. Introduction

In recent years, graphene shows great applications in photocatalysis and energy conversation fileds due to the unique sp^2 hybrid carbon network, high carrier mobility, large theoretical specific surface area and excellent thermal conductivity.[1-6] Generally, graphene oxide (GO) and reduced graphene oxide (RGO) exhibit many physicochemical properties similar to those of graphene. RGO can be prepared by reduction of GO, which improves greatly the electron conductivity of the materials.[7,8] RGO has been considered as an ideal support and an electron mediator to construct novel photocatalysts. Very recently, semiconductor/RGO photocatalysts were proved to possess extended the absorption in visible light region and promoted photocatalytic performance.[9-17] Numerous attempts have been made to combine RGO with semiconductor nanomaterials, such as TiO_2, Fe_2O_3, and WO_3.[9,10,18] An et al. reported that the WO_3-nanorods/RGO composites demonstrated significantly enhanced photocatalytic activity because of the improved separation efficiency of the photogenerated charges.[18] Various α-Fe_2O_3/graphene nanocomposites have also been synthesized by Parida's group and the optimized composite catalyst showed much higher photoactivity than that of the α-Fe_2O_3 nanorod.[19-22] However, for further improving the photocatalytic activity, designing and synthsizing novel graphene-based photocatalysts are still needed.

Indium oxide (In_2O_3) has been regarded as a nice candidate of photocatalysts for water splitting to produce hydrogen or organic pollutants decomposition owing to its narrow band gap energy (ca. 2.8 eV), stable physicochemical properties and low toxicity.[23-27] Despite the substantial merits, a major drawback of In_2O_3 is the fast recombination of photoexcited electron-hole pairs, leading to a relatively low photoactivity. Generally, well-crystallized nanocrystals with controlled size and shape as well as with the increased density of active sites are favourable for the electron transfer and photocatalytic reaction.[28-31] Recently, various In_2O_3 nanomaterials, such as nanowires, nanaocubes and nanorods, have been synthesized and used as photocatalysts because of their unique one dimensional nanostructure and promising functions.[32-34] Zhao et al. verified that In_2O_3 nanorods (INR) with high surface-to-volume ratio and single crystal structure could provide a direct path for the photoinduced charges transfer, resulting in enhanced photocatalytic activity.[34] However, to the best of our knowledge, the investigation about the composite prepared by hybridizing the one dimensional INR with RGO and its application for visible-light-driven photocatalysis has not been reported.

Herein, we report fabrication, characterization and photocatalysis of a novel hybrid composed of In_2O_3 nanorods (INR) and reduced graphene oxide (RGO). The nanohybrid (INR/RGO) was prepared through a two-step method: hydrothermal reaction for preparing In_2O_3 nanorods and UV-assisted reduction GO to RGO and then coupling with INR. The one dimensional INR was uniformly anchored on the surface of RGO and the two moieties of the composite exhibited nice interfacial contacts. In the INR-RGO composite, the RGO moiety acted as an electron collector and transporter synergistically enhanced electron transfer from INR to RGO and decreased the

recombination of electrons and holes, resulting in a greatly enhanced the photocatalytic activity of the degradation of 4-chlorophenol. Our research demonstrates a potential application of INR-RGO composite as a novel photocatalyst to remove environment contaminants.

2. Experimental

2.1. Materials.

$InCl_3 \cdot 4H_2O$ (A.R., 99.99%), urea and graphite powder (Alfa Aesar, 325 mesh, 99.9995%) were purchased and used without further purification.

2.2. Synthesis of INR-RGO.

In_2O_3 nanorods were prepared via hydrothermal method. In a typical procedure, 50 mL of $InCl_3$ (0.25 mol L^{-1}) solution was mixed with 50 mL of urea solution (2.4 mol L^{-1}) under magnetic stirring. Then the mixture was transferred into a 150 mL Teflon-lined stainless steel autoclave, and heated at 130 ºC for 12 h. The solid was collected by centrifugation and washed with distilled water and ethanol for several times, dried at 80 ºC for 24 h in air, then annealed in air at 350 ºC for 3 h, resulting in In_2O_3 nanorods (INR). Graphene oxide (GO) were synthesized using graphite powder as the starting material by a modified Hummers-method.[35]

INR/RGO nanohybrid was fabricated via an UV-assisted reduction and coupling method. In a typical experiment, a certain amount of GO solution (0.5 g L^{-1}), 0.2 g of INR and 50 mL of ethanol were added into a 100 mL cylindrical quartz glass vessel. The mixture was sonicated for 30 min, then, irradiated by a 500 W high pressure Hg lamp with the main wave crest at 365 nm for 8 h under magnetic stirring. After UV light irradiation, it was found that the color of suspension had changed into greyish-black, indicating the successful chemical reduction of GO to RGO. Finally, the mixture was filtered and the solid was rinsed by deionized water several times, and dried under vacuum at room temperature. The resulting samples were labelled as INR-RGO-x, where x stands for the weight percentage of RGO in the composite, which may vary from 0 to 5, depending on the ratio of the starting materials in the synthesis. For comparison, RGO was also prepared using the same UV-assisted reduction method.

2.3. Characterization.

X-ray diffraction (XRD) patterns of as-prepared samples were obtained on a Philips diffractometer using Ni-filtered Cu Kα radiation operating at 40 kV and 40 mA. The patterns were recorded in the range 10-80° (2θ). The samples for XRD analysis were prepared by dropping the suspension of the sample on a glass plate, which was dried under vacuum to form a thin film. Transmission electron microscopy (TEM) observation was conducted on a Philips TECNAI-12 instrument. The samples for TEM analysis were ultrasonically dispersed in EtOH for 30 min and ca. 3 μL of the resulting suspension was dropped onto carbon coated Cu grids, then allowed to air dry. Field emission scanning electron microscopy (FESEM) measurements were taken using a Hitachi S-4700 microscope. The Energy-dispersive X-ray (EDX) analysis was performed on a KEVEX X-ray energy detector. X-ray photoelectron spectroscopy (XPS) measurements were carried out an AXIS Ultra DLD system (Kratos Analytical Inc.) using monochromatic Al Kα radiation. All binding energies (BE) were referenced to the C1s peak at 284.6 eV. Fourier transform infrared (FTIR) spectra of the samples were obtained with Thermo Scientific Nicolet 6700 instrument. The solid samples were dried in vacuum at room temperature for 2 h, and then dispersed in KBr and compressed into a thin disk for the measurement. Raman spectra of the samples were measured with a JobinYvon HR-800 spectrometer using a He-Ne laser (λ = 633 nm, spot size ~ 1 mm). UV-vis diffuse reflectance spectra (DRS) of the samples were measured on a UV-1800 SPC spectrophotometer. Photoelectrochemical measurements of the samples were carried out on a CHI 660 B potentiostat/galvanostat electrochemical analyzer in a three-electrode system consisting of an indium tin oxide (ITO) glass covered with the sample, a platinum wire, and a Ag/AgCl electrode. The ITO covered the sample acted as a working electrode, the platinum wire as the counter electrode, and Ag/AgCl as reference electrode. The electrodes were immersed in 1 M of Na_2SO_4 solution. The working electrode was irradiated with a 150 W GY-10 xenon lamp during the measurement. A 400 nm cut-off filter was set between the lamp and the working electrode for the visible light irradiation. The electrochemical impedance spectroscopy (EIS) were carried out using a similar system for the measurement of photoelectrical response under the perturbation signal of 5 mV over the frequency range from 10 to 10 MHz.

2.4. Measurements of Photocatalytic Activities.

The photocatalytic degradation of 4-chlorophenol (4-CP) was carried out in a 50 mL quartz photochemical reactor containing 50 mL of 4-CP (25 mg L^{-1}) and the catalyst (C_{catal}=1.0 g L^{-1}). A water-cooling system was used to maintain the solution at the room temperature. The pH value of the system was adjusted by addition of hydrochloric acid or sodium hydroxide solution. The system was stirred continuously with air bubbling into the reaction solution and irradiated by a 150 W Xe lamp at 298 K and atmospheric pressure. The visible light irradiation was obtained from the xenon lamp equipped with a UV cut off filter (λ > 400 nm). During irradiation, ca. 1.5 mL of the suspension was taken from the reactor with a syringe at a regular time interval for analysis. The sample taken out of the reactor was centrifuged to separate the solid photocatalyst from the suspension. The solution was analyzed with a high pressure liquid chromatograph (P680ALPG4) equipped with a UVD170U analysis detector and a C18 column.

3. Results and discussion

3.1. Structure and Morphology of the Samples

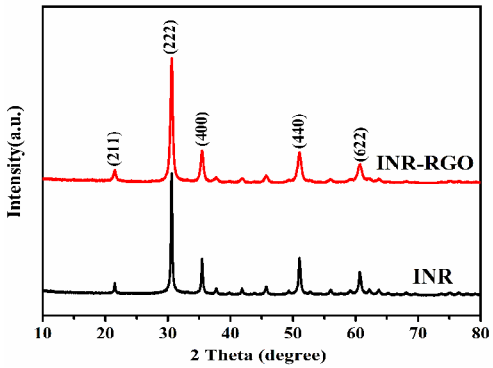

Fig. 1 Wide-angle XRD patterns of INR and the INR-RGO composite.

The crystalline phase and structure of the as-prepared samples were examined by powder X-ray diffraction (XRD). The XRD patterns of INR and the INR-RGO-2 composite are shown in Fig. 1. The peaks at 21.4°, 30.5°, 35.4°, 50.9° and 60.5° correspond to the (211), (222), (400), (440) and (622) planes of the cubic In_2O_3 (JCPDS No.71-2194).[36] Furthermore, no characteristic diffraction of carbon species has been detected from INR-RGO-2, which may attribute to the relatively low amount and weak intensity of RGO in the composite.[37]

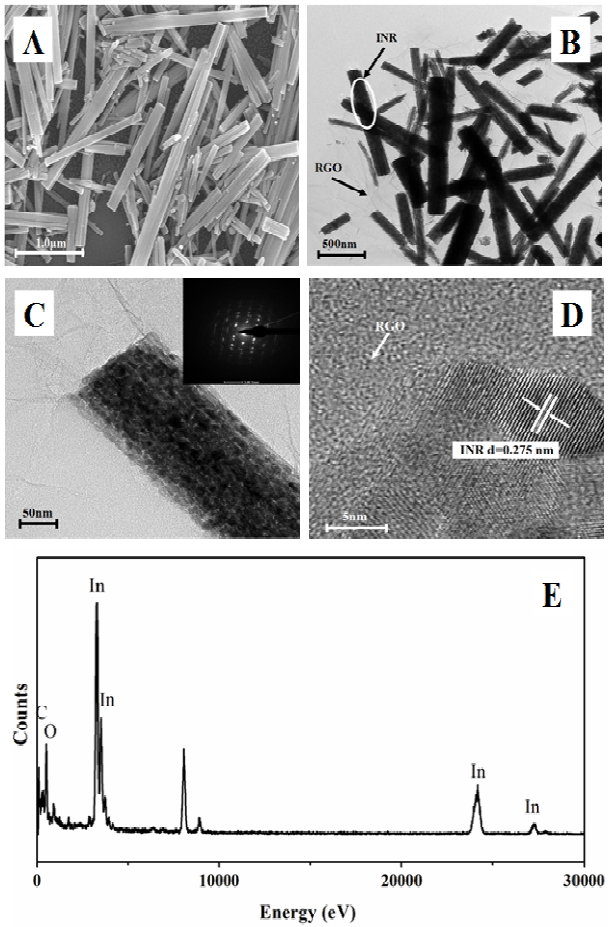

Fig. 2 SEM image of INR (A) and TEM image of INR-RGO composite (B, C); the selected area diffraction (SAED), HRTEM image (D) and EDX spectra of INR-RGO (E) composite.

SEM and TEM were taken to analyze the morphology and the microscopic structure of INR and INR-RGO-2, and the results are displayed in Fig. 2. It can be observed from Fig. 2A that the INR with a well-defined morphology are successfully synthesized. The as-prepared In_2O_3 demonstrated a rod-like shape with a diameter of ca. 200 nm and a length about 1.5~2.5 μm. As for INR-RGO-2 composite, the addition of RGO during the synthesis process did not affect the morphology of INR obviously. It can be seen from Fig. 2B that the INRs have homogeneously anchored on the RGO sheets, and the two-dimensional structure of RGO sheets with obvious wrinkles are still retained after the UV-assisted photoreduction treatment. The SAED pattern (inset Fig. 2C) recorded on the marked area of Fig. 2B reveals that INR possesses single crystal structure. As observed in the HRTEM (Fig. 2D), the measured lattice fringe spacing of 0.275 nm in INR-RGO-2 composite corresponds to the cubic INR.[34] Chemical composition analysis of INR-RGO-2 composite by EDX spectroscopy shows the presence of In, O and C elements in the composites (Fig. 2E), confirming that the obtained composite consists of RGO and INR.

3.2. XPS Analysis

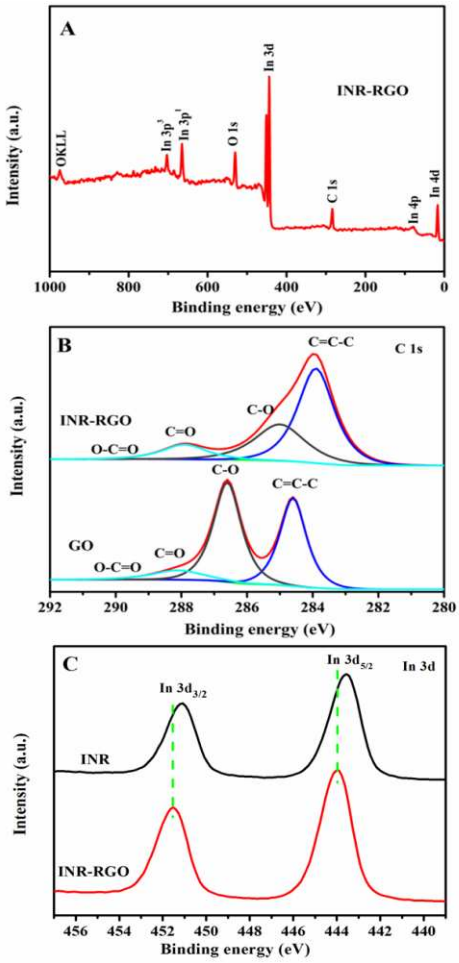

Fig. 3 XPS spectra of the (A) survey spectra of the INR and INR-RGO composite; (B) C 1s peaks of the GO and INR-RGO composite and (C) In 3d peaks of the INR and INR-RGO composite.

The XPS analysis was further employed to determine the

composition and the surface electronic state of the as-synthesized samples. Survey XPS spectrum (Fig. 3A) indicates that the INR-RGO-2 composite consists of C, In, and O elements. To investigate the degree of reduction of the RGO sheets in the composites, the high-resolution C1s spectrum of GO and INR-RGO are shown in Fig. 3B. Obviously, the C1s spectrum of GO can be deconvolved into four peaks corresponding to carbon atoms in different functional groups: the non-oxygenated ring C (284.6 eV), the C atom in the C–O bond (286.5 eV), the carbonyl C (C=O, 288.3 eV) and the carboxylate C (O–C=O, 289.1 eV).[38] After the hybridization with INR and the photoreduction treatment, the intensity of the C–O peak is dramatically decreased, indicating the GO have been reduced to RGO sheets. Fig. 3C shows the In 3d core level photoelectron spectra of INR and INR-RGO-2. The spectrum of INR sample may be fitted with two peaks corresponding to In $3d_{5/2}$ centered at 443.7 eV and In $3d_{3/2}$ at 451.1 eV, indicating the presence of In^{3+}.[19] Furthermore, the peak corresponding C–O in INR-RGO-2 composite (Fig. 3B) exhibited an obvious shift to lower binding energy position compared with that of the GO. Simultaneously, the fact that both the peaks of In $3d_{5/2}$ and $3d_{3/2}$ have a shift of 0.4 eV to the higher bonding energy (Fig. 3C) demonstrates chemical bonding between INR and RGO in the hybrid.[39] The chemical interaction between GO and INR may be attributed to the formation of In-O-C chemical bond. The similar phenomenon was also observed from TiO_2-RGO systerm.[40]

3.3. FTIR and Raman Spectra.

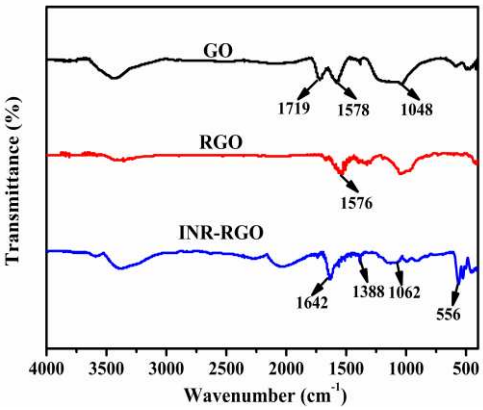

Fig. 4 FTIR spectra of GO, RGO and INR-RGO composite.

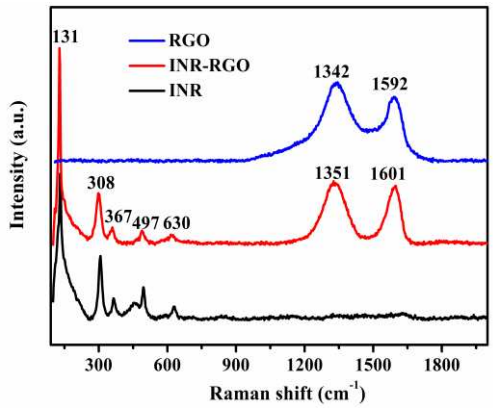

Fig. 5 Raman spectra of RGO, INR and INR-RGO composite.

The FTIR spectra of the samples are shown in Fig. 4. The characteristic absorption bands of GO are observed at 1048 (C–OH), 1578 (C=C) and 1719 cm^{-1} (C=O). For the photoreduced RGO, the intensity of the absorption bands corresponding to C–OH and C=O groups decreases significantly, and the absorption band corresponding to C=C vibration slightly red-shifts to 1576 cm^{-1}. For the INR-RGO-2 hybrid, the broad IR band at low frequency reflect the stretching vibration of In-O-In bonds, and the bond at 556 cm^{-1} might be assigned to In–O vibration.[41] Moreover, the peaks corresponding to C=O and C–OH vibrations at 1719 and 1048 cm^{-1} in the INR-RGO-2 composite are not observed and a new absorption band appeared at 1642 cm^{-1}, which might be attributed to the skeletal vibration of the RGO sheets.[42] These results indicate that the oxygen functional groups in GO were removed and GO was reduced during the formation of INR-RGO-2 composite.[43]

The interaction between INR and RGO was confirmed by the Raman spectral analysis (Fig. 5). For INR, the five distinct peaks located at 131, 308, 367, 497, and 630 cm^{-1} could be detected. As is expected, RGO displays two prominent G and D bands, which are generally assigned to the E_{2g} photon of sp^2 bonds of carbon atoms, and a breathing mode of κ-point phonons of A_{1g} symmetry, respectively.[44] Compared with RGO sheets, it could be observed that the D- and G-band of INR-RGO-2 slightly up-shifts to 1351 cm^{-1} and 1601 cm^{-1}, respectively, which provides another evidence of superior interactions between INR and RGO.

3.4. Optical and Photoelectrochemical Properties of the Samples.

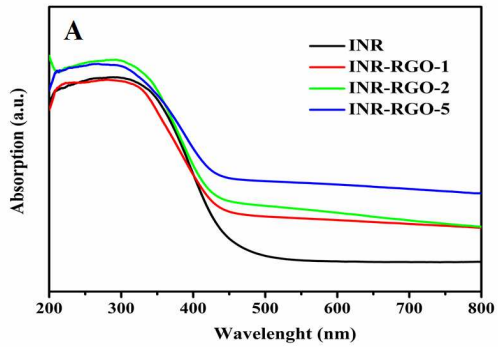

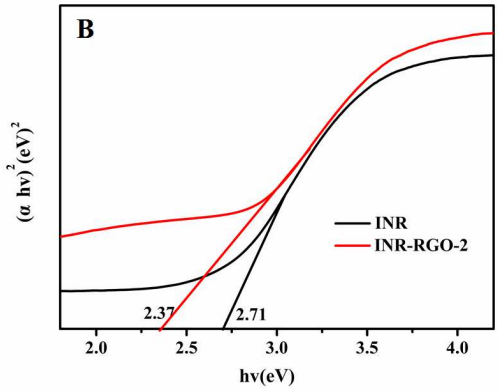

Fig. 6 (A) UV-vis diffuse reflectance spectra of the as-prepared INR, INR-RGO-1, INR-RGO-2 and INR-RGO-5 composites. (B) The plots of $(ahv)^2$ versus energy hv for INR and INR-RGO-2 composite.

The UV-vis diffuse reflectance spectra of INR and INR-RGO-x composites with various contents of RGO are shown in Fig. 6A. It can be seen that the absorption intensity of INR-RGO-x composites increases with the augment of RGO content. The red-shift of the absorption edge of INR-RGO-x composites may be ascribed to some restoration of the π-π conjugation network of the RGO in the hybrid.[45] Moreover, Fig. 6B shows the plots of $(\alpha h\nu)^2$ versus photon energy, which show that the band gap of the INR is 2.71 eV, whereas the band gap of the INR-RGO-2 composite has been consequently reduced to 2.37 eV. The narrowing of the band gap in the case of INR-RGO-2 composite was attributed to the interaction between INR and RGO. Therefore, hybridization of INR and RGO to form a composite may also change band gap and light absorption property of the materials.

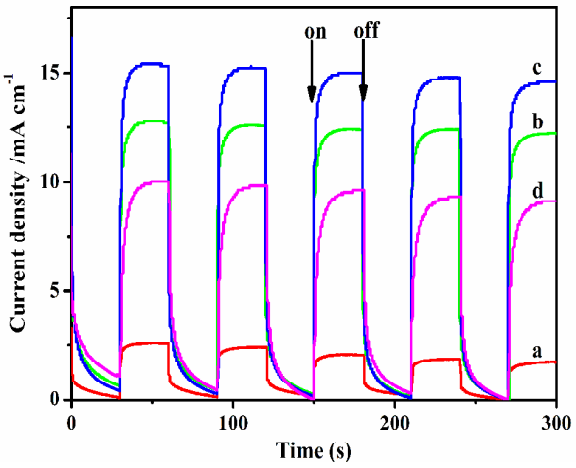

Fig. 7 Photocurrents of (a) INR, (b) INR-RGO-1, (c) INR-RGO-2 and (d) INR-RGO-5 under visible light irradiation (λ > 400 nm) at 1.2 V. The power of the lamp with a 400 nm cut-off filter is ca. 100 mW/cm^2.

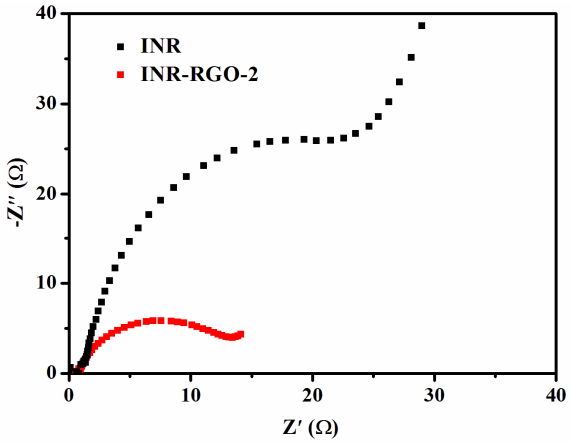

Figure 8 Nyquist plots of electrochemical impedance spectra (EIS) for the electrodes covered with INR and INR-RGO-2 composites in 0.5 M Na_2SO_4 electrolyte.

The results of photoelectrochemical experiments performed under visible light illumination are shown in Fig. 7. Under visible light irradiation (λ > 400 nm) and 1.2 V applied voltage, blank experiments conducted with the bare ITO electrode do not produce photocurrent. It is found that the INR electrode demonstrated prompt but weak photocurrent responses under visible light irradiation. However, obviously enhanced photocurrent responses for INR-RGO electrodes are detected. As the content of RGO in the INR-RGO composites increased from 1% to 2 wt%, the corresponding the photocurrent density increased from 12.23 to 15.41 mA cm^{-2}. The order of photocurrent response is INR-RGO-2 > INR-RGO-1 > INR-RGO-5 > INR. The maximum photocurrent density for INR-RGO-2 electrode is ca. 6 times as high as that of INR electrode under the same irradiation conditions, suggesting that positive synergetic effect between INR and RGO components in the hybrid. The enhancement of the photocurrent for INR-RGO electrodes indicates higher charge separation efficiency and the prolonged lifetime of the photogenerated electrons and holes. With the extensive two-dimensional π-π conjugation structure, RGO serves as an acceptor and transporter of the electrons generated from the In_2O_3 semiconductor, which enhances the photogenerated charges separation.[46]

Electrochemical impedance spectrum (EIS) is another powerful tool to study the charge transfer process. As shown in Figure 8, the radius of the Nyquist curve of INR-RGO-2 is much smaller than that of INR, indicating the fast interfacial electron transfer between INR and RGO and efficient hindrance of the charge recombination in the hybrid.[47]

3.5. Photocatalytic Activity.

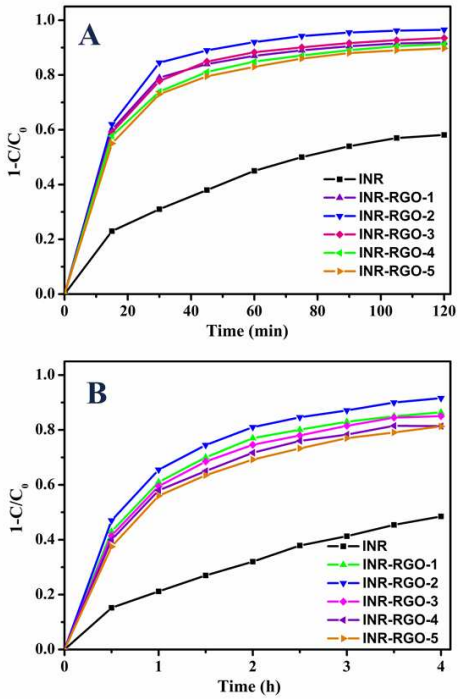

Fig. 9 Photodegradation 4-CP yields over the as-prepared INP, INR and INR-RGO-x composites under UV-vis light (A) and visible light (B) (λ > 400 nm) irradiation. *Reaction conditions: $m_{catalyst}$ = 50 mg, T = 298 K, pH = 3,light source:150 W Xe lamp (a cut-off filter (λ > 400 nm) used for visible light irriadiation*).

The photocatalytic degradation of 4-CP was investigated under UV-vis and visible light (>400 nm), respectively. From Fig. 9A we can see that the 4-CP photodegradation yield of INR is 58.1% after 2 h UV-vis light irradiation. However, the 4-CP photodegradation yields of INR-RGO-1 reached 91.9%. In addition, along with the increase of RGO in the composite, the photocatalytic activity of INR-RGO composites reached to a summit then decreased. The optimized RGO content in the INR-RGO composite is *ca*. 2 wt% and the 4-CP degradation yield of the catalyst under 2h UV-vis irradiation is 96.2%, which gives approximately 38% increase compared with that of INR in the same conditions.

In order to further investigate the photocatalytic properties of the as-prepared samples, analogous experiments are conducted under visible light irradiation ($\lambda > 400$ nm). As shown in Fig. 9B, the 4-CP photodegradation yield of INR-RGO-2 under 4 h visible-light irradiation is ca. 91.6 %, which is ca. 1.9 times as high as that of INR under the similar conditions. These results demonstrate that the INR-RGO composites possess very nice visible-light photocatalytic activity for photodegradation of 4-CP.

In general, the enhancement of photocatalytic activity of INR-RGO under UV-vis or visible-light irradiation for 4-CP degradation could be attributed to the excellent electronic conductivity and large specific surface area of RGO,[3] which enhances the photoinduced electrons transport from INR to the RGO sheets, thus, inhibits the recombination of photoinduced electrons and holes.

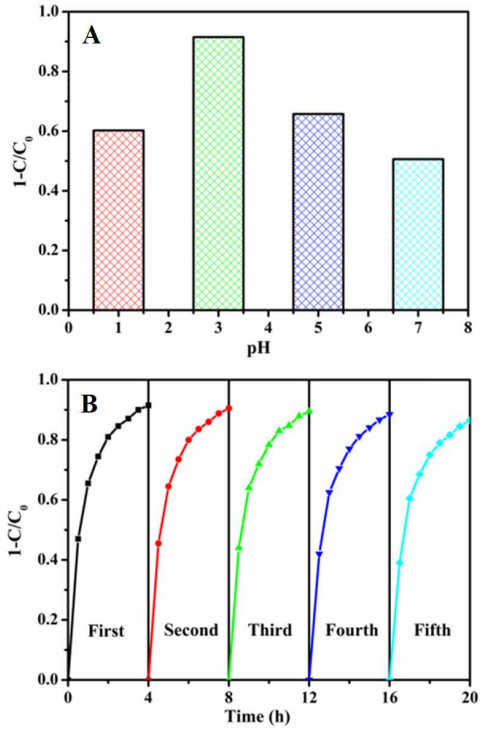

Fig. 10 Effect of the pH values on photodegradation of 4-CP under visible light (A) and Cycling measurements of the yields of 4-CP degradation under visible light irradiation (B) by INR-RGO-2 composite. *Reaction conditions: $m_{catalyst}$ = 50 mg, T = 298 K, pH = 3, light source:150 W Xe lamp with cut-off filter (λ > 400 nm).*

Fig. 10A shows the effect of the pH values on the photodegradation yields of 4-CP under visible light irradiation. The pH value of the system influences the photodegradation yields of 4-CP dramatically. When pH value varies from 1 to 7, the maximum average photodegradation yield of 4-CP was achieved at a pH of 3. The reason that organic contaminants photodegradation should occur at an optimized pH may be attributed to that the concentration of H^+ in the solution may influence the transfer of photoinduced electrons and redox potential of the contaminant, thus, affect the photocatalytic activity of the catalyst.[48, 49]

The stability of INR-RGO-2 composite for the photodegradation of 4-CP is shown in Fig. 10B. The results of five cycles of photocatalytic experiments demonstrated that the INR-RGO-2 composite is very stable and thus suitable for treatment of organic contaminants in wastewater.

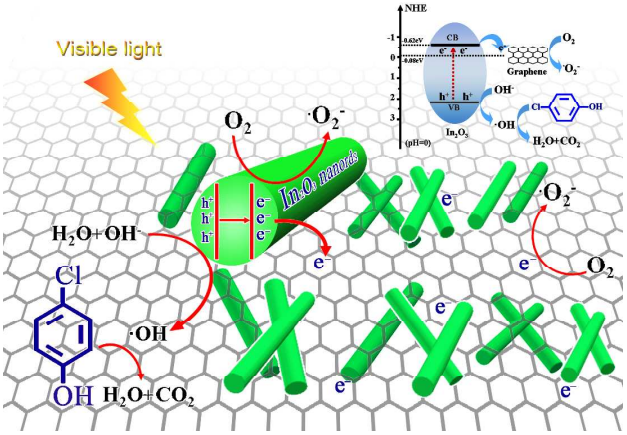

Scheme 1 Schematic photoexcited electron transfer and 4-CP degradation over the INR-RGO photocatalyst under visible light irradiation.

According to the above results, the photocatalytic mechanism is illustrated in Scheme 1. Photodegradation of 4-CP is believed to be initiated by ·OH radicals. In the presence of O_2, the ·OH radicals are generated in the following photochemical reactions:

$$In_2O_3 + h\nu \rightarrow In_2O_3\ (e^- + h^+) \quad (1)$$

$$In_2O_3\ (e^-) + RGO \rightarrow In_2O_3 + e^-\ (RGO) \quad (2)$$

$$e^- + O_2 \rightarrow \cdot O_2^- \quad (3)$$

$$2\cdot O_2^- + 2H_2O \rightarrow H_2O_2 + O_2 + 2OH^- \quad (4)$$

$$H_2O_2 \rightarrow 2\cdot OH \quad (5)$$

$$h^+ + H_2O \rightarrow \cdot OH + H^+ \quad (6)$$

$$h^+ + OH^- \rightarrow \cdot OH \quad (7)$$

$$4\text{-CP} + \cdot OH \rightarrow CO_2 + H_2O \quad (8)$$

Under UV-vis or visible light illumination, electrons (e^-) can be excited from the valence band (VB) to the conduction band (CB) of INR, producing the same amount of holes (h^+) in the VB of the semiconductor. The photogenerated electrons in the conduction band of INR transfer to RGO and then react with oxygen molecules dissolved in the solution to yield superoxide $\cdot O_2^-$ and finally form ·OH, which may play a major role in the photodegradation of 4-CP.[50,51] Meanwhile, 4-CP

molecules may also be oxidized by the holes immigrating to the surface of INR.

4. Conclusions

In summary, the INR-RGO composite, as a novel photocatalyst, was successfully prepared by a facile UV-assisted photoreduction method. Importantly, with the one dimensional INR anchored uniformly on the RGO sheets, the as-synthesized INR-RGO composites displayed effective interfacial contact between INR and RGO, resulting in excellent photocatalytic activity for the degradation of 4-CP. The enhancement of photocatalytic activity can be attributed to INR with high surface-to-volume ratio providing a direct path for photoinduced charge transfer as well as the unique properties of RGO, which acts as an electron collector and transporter synergistically enhanced electron transfer from INR to RGO and suppressed the recombination of electron-hole pairs, leading to a enhanced the photocatalytic activity of the degradation of 4-CP. The present study provides an example for designing and preparation of graphene-based hybrid materials for the photodegradation of organic pollutants.

Acknowledgements

The authors gratefully acknowledge financial support of this research by the National Natural Science Foundation of China (21373143 and 51273141), the Priority Academic Program Development of Jiangsu Higher Education Institutions (PAPD), the Project of Scientific and Technologic Infrastructure of Suzhou (SZS201207), and Qing Lan Project of Jiangsu Province.

Notes and references

[a] *College of Chemistry, Chemical Engineering and Materials Science, Soochow University, Suzhou 215123, China. Fax: +86-512-6588 0089; Tel.: +86-512-6588 0361; E-mail address: pyang@suda.edu.cn.*
[b] *Suzhou Institute of Nano-tech and Nano-bionics, Chinese Academy of Sciences, Suzhou 215123, China*
[c] *Department of Chemistry, Nantong Vocational University, Nantong 226007, China*

†Electronic Supplementary Information (ESI) available. See DOI: 10.1039/b000000x/

1. A. K. Geim and K. S. Novoselov, *Nat. Mater.*, 2007, **6**, 183.
2. A. Dato, V. Radmilovic, Z. Lee, J. Phillips and M. Frenklach, *Nano Lett.*, 2008, **8**, 2012.
3. A. A. Balandin, S. Ghosh, W. Bao, I. Calizo, D. Teweldebrhan, F. Miao and C. N. Lau, *Nano Lett.*, 2008, **8**, 902.
4. X. Q. An and J. C. Yu, *RSC Adv.*, 2011, **1**, 1426.
5. Q. J. Xiang, J. G. Yu and M. Jaroniec, *Chem. Soc. Rev.*, 2012, **41**, 782.
6. S. Stankovich, D. A. Dikin, G. H. Dommett, K. M. Kohlhaas, E. J. Zimney, E. A. Stach, R. D. Piner, S. T. Nguyen and R. S. Ruoff. *Nature*, 2006, **442**, 282.
7. X. Huang, X.Y. Qi, F. Boey and H. Zhang, *Chem. Soc. Rev.*, 2012, **41**, 666.
8. J. X. Zhu, D. Yang, Z. Y. Yin, Q. Y. Yan and H. Zhang, *Small*, 2014, 1.
9. S. Guo, G. K. Zhang, Y. D. Guo and J. C. Yu, *Carbon,* 2013, **60**, 437.
10. S. D. Perera, R. G. Mariano, K. Vu, N. Nour, O. Seitz, Y. Chabal and K. J. Balkus, *ACS Catal.*, 2012, **2**, 949.
11. Z. Chen, S. Liu, M. Q. Yang and Y. J. Xu, *ACS Appl. Mater. Interfaces,* 2013, **5**, 4309.
12. H. Zhang, X. J. Lv, Y. M. Li, Y. Wang and J. H. Li, *ACS Nano*, 2009, **4**, 380.
13. O. Akhavan, *ACS Nano*, 2010, **4**, 4174.
14. Y. H. Ng, A. Iwase, A. Kudo and R. Amal, *J. Phys. Chem. Lett.,* 2010, **1**, 2607.
15. W. Zhao, W. H. Ma, C. C. Chen, J. C. Zhao and Z. G. Shuai, *J. Am. Chem. Soc.*, 2004, **126**, 4782.
16. S. Liu, J. Q. Tian, L. Wang, Y. L. Luo and X. P. Sun, *Catal. Sci. Technol.,* 2012, **2**, 339.
17. S. M. Sun, W. Z. Wang and L. Zhang, *J. Phys. Chem. C*, 2013, **117**, 9113.
18. X. Q. An, J. C. Yu, Y. Wang, Y. M. Hu, X. L. Yu and G. J. Zhang, *J. Mater. Chem.*, 2012, **22**, 8525.
19. D. K. Padhi and K. Parida, *J Mater. Chem. A*, 2014, **2**, 10300.
20. S. Martha, D. K. Padhi and K. Parida, *ChemSusChem*, 2014, **7**, 585.
21. D. K. Padhi, G. K. Pradhan, K. M. Parida and S. K. Singh, *Chem. Eng. J.*, 2014, **255**, 78.
22. G. K. Pradhan, D. K. Padhi and K. M. Parida, *ACS Appl. Mater. Interfaces,* 2013, **5**, 9101.
23. J. B. Mu, C. L. Shao, Z. C. Guo, M. Y. Zhang, Z. Y. Zhang, P. Zhang, B. Chen and Y. C. Liu, *J. Mater. Chem.*, 2012, **22**, 1786.
24. F. Di Quarto, C. Sunseri, S. Piazza and M. C. Romano, *J. Phys. Chem. B*, 1997, **101**, 2519.
25. G. D. Liu, D. R. Chen and X. L. Jiao, *CrystEngComm*, 2009, **11**, 1828.
26. J. Lee, T. Park, J. Lee, S. Lee, H. Park and W. Yi, *Carbon*, 2014, **76**, 378.
27. A. Walsh, J. L. F. Da Silva, S. H. Wei, C. Körber, A. Klein, L. F. J. Piper, A. DeMasi, K. E. Smith, G. Panaccione, P. Torelli, D. J. Payne, A. Bourlange and R. G. Egdell, *Phys. Rev. Lett.*, 2008, **100**, 167402.
28. Y. Li and W. J. Shen, *Chem. Soc. Rev.*, 2014, **43**, 1543.
29. W. J. Zhou, H. Liu, R. I. Boughton, G. J. Du, J. J. Lin, J. Y. Wang and D. Liu, *J. Mater. Chem.*, 2010, **20**, 5993.
30. Y. Sakatani, D. Grosso, L. Nicole, C. Boissiere, G. J. de A. A. Soler-Illia and C. Sanchez, *J. Mater. Chem.*, 2006, **16**, 77.
31. H. Huang, C. Wang, J. Huang, X. M. Wang, Y. K. Du and P. Yang, *Nanoscal*, 2014, **6**, 7274.
32. Q. Wan, M. Wei, D. Zhi, J. L. MacManus-Driscoll and M. G. Blamire, *Adv. Mater.*, 2006, **18**, 234.
33. Q. S. Liu, W. G. Lu, A. H. Ma, J. K. Tang, J. Lin and J. Y. Fang, *J. Am. Chem. Soc.*, 2005, **127**, 5276.
34. J. J. Zhao, M. B. Zheng, X. Y. Lai, H. L. Lu, N. W. Li, Z. X. Ling and J. M. Cao, *Mater. Lett.*, 2012, **75**, 126.
35. W. S. Hummers and R. E. Offeman, *J. Am. Chem. Soc.*, 1958, **80**, 1339.
36. H. Zhu, X. L. Wang, L. Qian, F. Yang and X. R. Yang, *J. Phys. Chem. C*, 2008, **112**, 4486.
37. D. W. Chu, Y. Masuda, T. Ohji and K. Kato, *Langmuir*, 2010, **26**, 14814.
38. H. Huang, Z. K. Yue, G. Li, X. M. Wang, J. Huang, Y. K. Du and P. Yang, *J. Mater. Chem. A*, 2013, **1**, 15110.
39. R. A. Rakkesh, D. Durgalakshmi and S. Balakumar, *J. Mater. Chem. C*, 2014, **2**, 6827.
40. L. C. Liu, Z. Liu, A. N. Liu, X. R. Gu, C. Y. Ge, F. Gao and L. Dong, *ChemSusChem*, 2014, **7**, 618.
41. C. L. Chen, D. R. Chen, X. L. Jiao and C. Q. Wang, *Chem. Commun.*, 2006, 4632.
42. Q. Li, B. D. Guo, J. G. Yu, J. R. Ran, B. H. Zhang, H. J. Yan and J. R. Gong, *J. Am. Chem. Soc.*, 2011, **133**, 10878.
43. J. W. Qin, M. H. Cao, N. Li and C. W. Hu, *J. Mater. Chem.*, 2011, **21**, 17167.
44. K. N. Kudin, B. Ozbas, H. C. Schniepp, R. K. Prud'homme, I. A. Aksay and R. Car, *Nano Lett.*, 2007, **8**, 36.
45. X. J. Bai, L. Wang, R. L. Zong, Y. H. Lv, Y. Q. Sun and Y. F. Zhu, *Langmuir*, 2013, **29**, 3097.
46. J. G. Hou, Z. Wang, W. B. Kan, S. Q. Jiao, H. M. Zhu and R. V. Kumar, *J. Mater. Chem.*, 2012, **22**, 7291.
47. X. Yan, Y. J. Li, F. Du, K. Zhu, Y. Q. Zhang, A. Y. Su, G. Chen and Y. J. Wei, *Nanoscale*, 2014, **6**, 4108.

48. F. D. Kopinke, K. Mackenzie, R. Koehler and A. Georgi, *Appl. Catal. A-Gen.*, 2004, **271**, 119.
49. T. Vincent, S. Spinelli and E. Guibal, *Ind. Eng. Chem. Res.*, 2003, **42**, 5968.
50. X. Wang, L. J. Zhi and K. Mullen, *Nano Lett.*, 2007, **8**, 323.
51. Y. C. Chen, Y. C. Pu, Y. J. Hsu, *J. Phys. Chem. C*, 2012, **116**, 2967.

Graphical Abstract

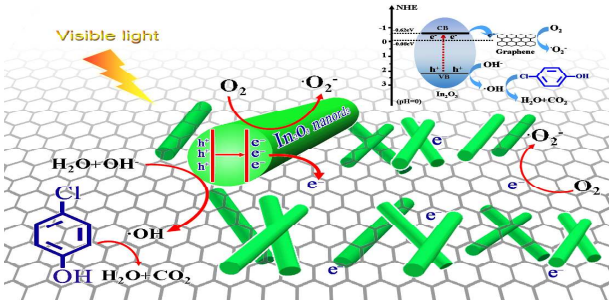

UV-assisted fabrication of In_2O_3 nanorods/reduced graphene oxide composites with enhanced interfacial charge transfer and photocatalytic performance under visible light